nEDM Research and Development Achievements

11/4/2011

Table of Contents

1 Introduction

The goal of the nEDM experiment is to improve the sensitivity for detecting a static neutron electric dipole moment by two orders of magnitude. The experimental approach being pursued was proposed by Golub and Lamoreaux [1]. Stripped to its essentials, this approach requires creating a three-component fluid (isotopically purified Helium-4, a trace amount of spin-polarized Helium-3, and spin-polarized ultracold neutrons) and subjecting it to a small, homogeneous magnetic field and a large electric field. A non-zero EDM would be revealed by a difference in the neutron precession frequency that has a linear dependence on the magnitude of the electric field strength, and whose sign depends on the relative alignment of the electric and magnetic fields.

Generally speaking, an attempt to improve a measurement by two orders of magnitude will require significant improvement to existing technologies. This was recognized at the start of the nEDM experiment, and as a result a significant R&D effort was undertaken. Significant progress has been made, and that is the focus of this report.

This report is organized as follows: Section 2 discusses the creation and storage of a large density of highly polarized UCNs; Section 3 discusses the creation, transport and storage of a sufficient density of highly polarized Helium-3 atoms; Section 4 discusses generating, maintaining, and monitoring the electric field; Section 5 discusses the stringent uniformity requirements of the magnetic fields; Sections 6 and 7 discuss the challenges of the neutron-capture and Helium-3 signal detection, respectively; Section 8 discusses an assortment of cryogenic mechanical challenges; Section 9 discusses experiments to better understand the geometric phase – the key systematic error for the experiment; Section 10 discusses progress in experimental simulation.

2 Neutrons

There are several challenges associated with obtaining a sufficient density and polarization of ultracold neutrons:

1. The neutron guide must be designed to achieve the maximum possible fluence and polarization of 8.9 Å neutrons, that subsequently interact with phonons in the liquid Helium-4 and down-scatter to an energy of the order of 100 neV.
2. Prompt-γ backgrounds must be sufficiently low that they do not unacceptably discharge the HV electrodes.
3. The neutron polarization must be maintained through the transition to the low-field region of the measurement cell.
4. The neutrons must pass through two thick vacuum windows that must be non-metallic due to eddy current heating and Johnson noise.
5. The neutrons must be stored in a material bottle for times comparable to the β-decay half-life (~1,000 seconds).

2.1 Neutron Guide

The neutron guide, a ballistic design with a bender polarizer and a splitter, has been optimized. McStas and GEANT4 simulations of the FnPB beamline have been carried out. Input neutron distributions, consistent with measured distributions, were incorporated into the simulation, as were realistic reflectivities in the guide segments. The flux (9.8 x 10^6 n/s/cm^2/Å) and polarization (95%) predicted by the two simulations are in good agreement; these values are assumed in the experimental sensitivity estimate.

Simulated neutron loss spectra, needed as input to shielding calculations, were also generated. Resulting γ-backgrounds can be effectively eliminated by using a Boron-free guide substrate and surrounding the guide with a Lithium blanket.

2.2 Neutron Spin-Holding Coils

Neutron spin-holding coils are needed to transport the neutrons into the measurement cell without losing polarization. The design of these magnets is complicated by the requirement that their fields not interfere with the main experimental field.

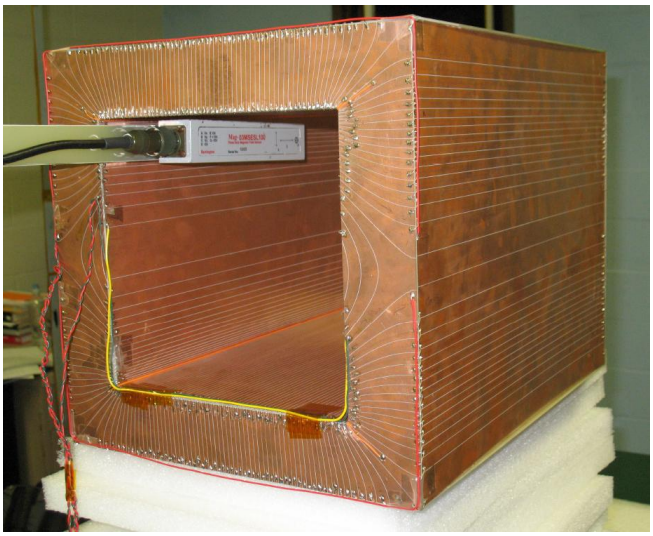

Figure 1: Prototype neutron spin holding coil with mapper.

To obtain an acceptable design, standard techniques have been inverted: the physical and magnetic boundary conditions are specified first, which then allows the required current distributions to be calculated [2]. These current distributions are then implemented as non-

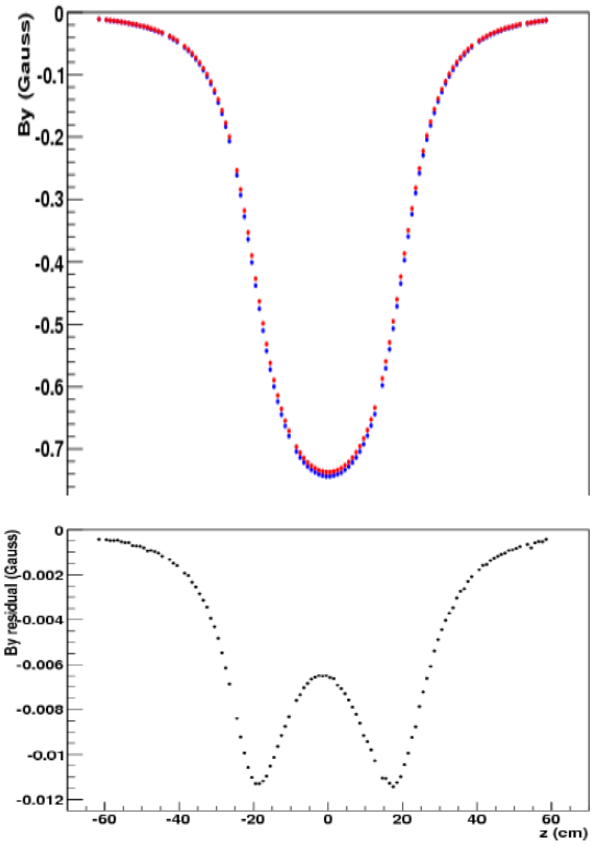

Figure 2: The vertical component of the magnetic field along the coil's central axis. Blue points show measured data, red points show theoretical results, and black points show the difference.

uniform traces on copper-plated G-10 plates, which are soldered together to form the necessary coils. A small prototype spin-holding coil (Figure 1) was successfully tested. Detailed magnet maps of the actual fields agreed with expectations to better than 1% over most of the coil volume (Figure 2). Calculations were performed to derive construction tolerances, which should be easily achievable.

A new method of construction of coils with cylindrical geometry has been developed. A solid G-10 form will be electroplated with copper on all surfaces. Trace boundaries will then be machined into the surface using a 3D CNC milling machine. This method simplifies construction and eliminates the current density uncertainty resulting from solder connections between traces on adjacent edges. This technique is also applicable to magnets needed to transport polarized Helium-3 atoms.

2.3 Neutron Windows

The incoming neutron beam must pass through two vacuum windows within the experiment's metal-exclusion zone: one at the boundary of the cryovessel and one at the entrance to the central volume which contains the liquid helium.

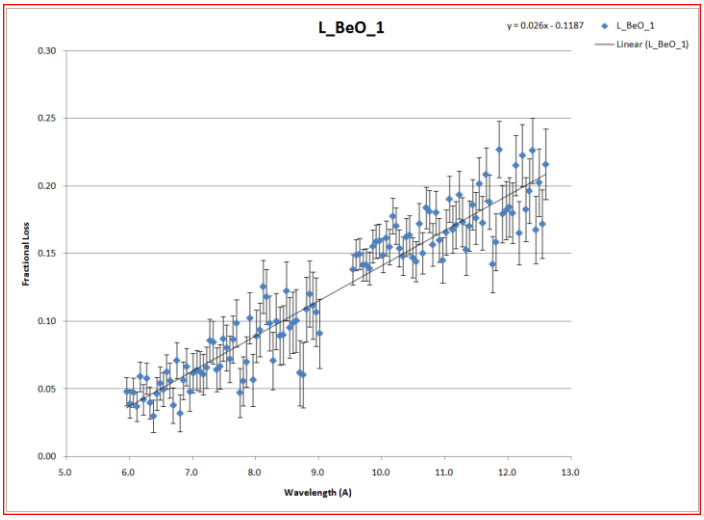

Figure 3: Results for neutron loss vs. wavelength for a 3/8" thick BeO sample.

Single-crystal silicon, quartz (single-crystal and fused) and Beryllium Oxide (BeO) were identified as candidate materials. Single-crystal silicon has questionable mechanical properties, single-crystal quartz is unavailable in required sizes, fused quartz was measured and found to have an unacceptable degree of neutron scattering. Results for neutron scattering measurements through a 3/8"-thick sample of BeO are shown in Figure 3 [3]. There is a linear increase of the scattering loss as a

function of wavelength; a fit to the data gives 11.3% loss at 8.9 Å. Calculations show that the BeO vacuum windows each need to be roughly 1/8" thick, so the total scattering through these windows is expected to be ~7.5%. This is likely an overestimate of the neutron loss through these windows since the collimator settings used to define lost neutrons were quite narrow.

2.4 Neutron Storage

The measurement cell walls must be coated with a material that converts the XUV scintillation light into visible light. This material must have a high UCN storage potential (it must also preserve Helium-3 spin (Section 3.3), must not scatter the produced light (Section 6.2), must be non-magnetic and must not activate). Deuterated tetraphenyl butadiene (dTPB) dissolved in deuterated polystyrene (dPS) has been shown to be a neutronically suitable material in the NIST lifetime experiment [5], but coating and construction techniques are complicated by the measurement cells' rectangular geometry.

Test cells, coated with dPS have been constructed and tested at the LANL UCN source (Figure 4). Recent results show fairly good wall loss per bounce (τ_{wall} > 1000 s) [4]. However, scans of a pre-polarizer magnet upstream of the storage cell show that the energy of the stored neutrons is below 50 neV, in seeming contradiction to the surface reflectivity measurements which give the expected storage potential (160 neV). The data are consistent with a small area where the coating material is thin enough (<50 nm) to allow quantum mechanical tunneling to the underlying, protonated, substrate.

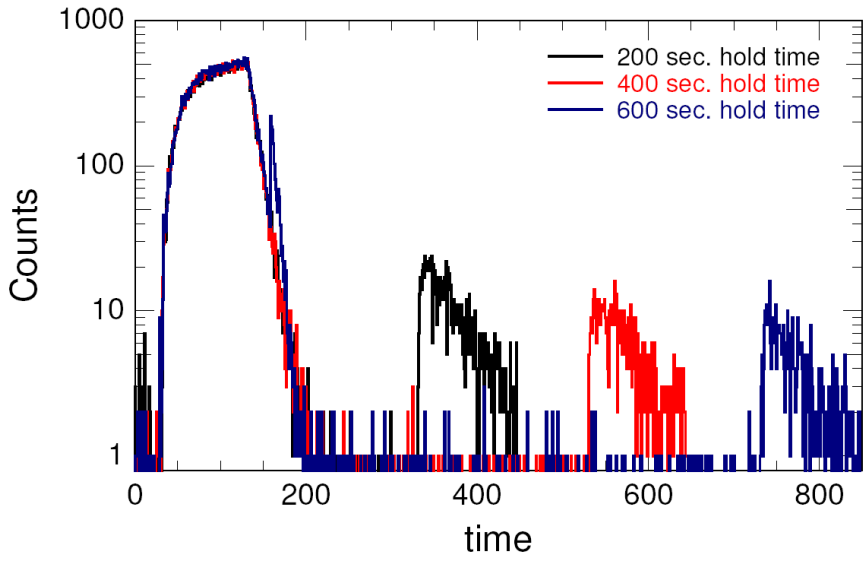

Figure 4: UCN storage data from a dPS coated test cell. The initial rise in counts is the signal while the UCN source is on and the cell valve is open. After closing the cell valve (at 130 sec.), the storage time is measured by counting the remaining UCN in the cell for different hold times.

3 Helium-3

There are several challenges associated with obtaining sufficient Helium-3 density and polarization:

1. An atomic beam source of highly polarized Helium-3 is required.
2. The beam must be injected into a volume of isotopically purified Helium-4.
3. The Helium-3 atoms must be moved from the injection volume, to the measurement cell. Then, after each measurement cycle (~30 minutes), the Helium-3 atoms must be removed.
4. During the process of moving between the injection volume and the measurement cell the Helium-3 atoms must not lose their polarization, either due to non-adiabatic changes in the magnetic field, or due to depolarizing interactions with surface materials.

3.1 ABS

In order to achieve sufficient Helium-3density and polarization, an atomic beam source (ABS), that works by filtering a beam of Helium-3 in a magnetic field gradient, was designed, built and tested [6] (Figure 4). A flux of 1.5×10^{14} atoms/s, and polarization of 99.5% (both of which exceed experiment requirements) were obtained.

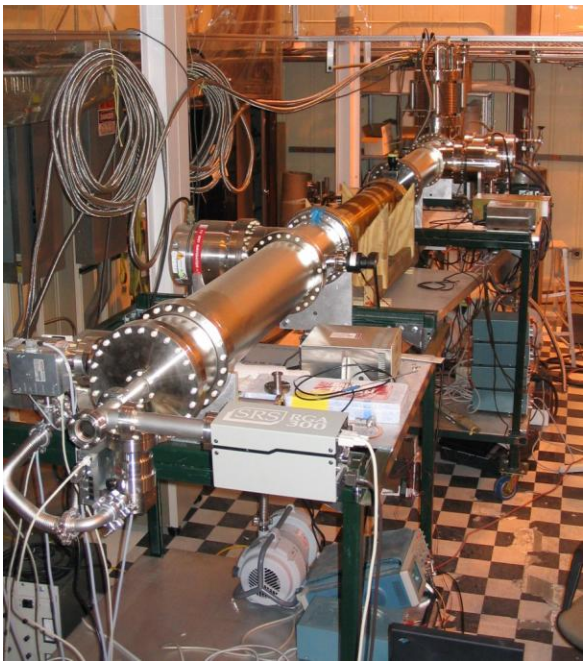

Figure 5: Photograph of nEDM atomic beam source.

3.2 Heat Flush

In order to move Helium between two volumes a temperature gradient must be established. The mass diffusion coefficient of Helium-3 in superfluid Helium-4 was measured in the operating temperature range, lower temperatures than measured previously, using a neutron beam to tomographically map the distribution of Helium-3 atoms subjected to heat currents [7]. This allowed calculation of the temperature gradients, given assumptions about wall interactions and the concentration dependence of the diffusion constant [8] needed to achieve the desired Helium-3 concentration. From this information the required heat load to the dilution refrigerator (DR) could be calculated, and was shown to be within the DR design parameters [9].

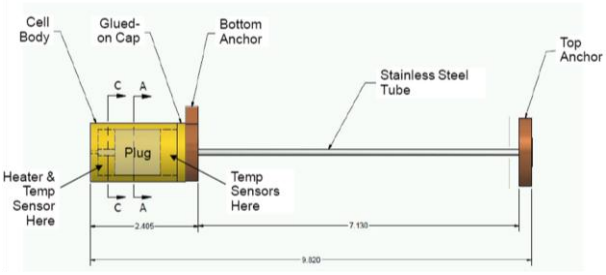

Figure 6: Adjustable Thermal Link test apparatus. The temperature difference across the plug (lower left) gives the thermal conductivity of the helium annulus between the plug and the test cell body.

An apparatus was developed (Figure 6) to test the concept of establishing such a gradient with an adjustable thermal link (ATL) implemented as a

variable-length annular region of liquid Helium (the longer the region, the less the thermal conductivity). Data (thermal conductance vs. temperature) along with theoretical calculations, are shown in Figure 7 [10].

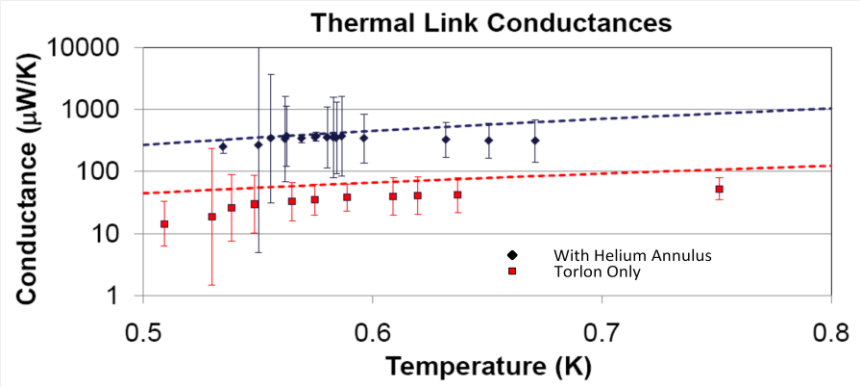

Figure 7: Measured (points) and expected (dashed lines) conductance vs. temperature for the test setup which is similar to an adjustable thermal link in the closed position ("With Helium Annulus"). Also plotted, as a check on the method, is the conductance measured with no helium present ("Torlon Only"), which is an order of magnitude smaller.

3.3 Material Depolarization

Measurements of the depolarization probability per bounce (P_d) were carried out as a function of temperature for 1) acrylic coated with dTPB-dPS (the measurement cell coating material), 2) Torlon, 3) Torlon coated with polyimide (the primary 3HeS plumbing material) and 4) BeCu coated with polyimide (used in 3HeS bellows) [11]. Results are shown in Table 1 and Figure 8. Calculations predict a resulting polarization loss of 1.5% during the transfer into the measurement cell due to wall loss.

Table 1: Average depolarization probability per bounce on various surfaces.

Material	~P_d
Acrylic coated with dTPB-dPS	1.0×10^{-7}
Bare Torlon 4203	1.0×10^{-6}
BeCu coated with Polyimide	8×10^{-7}
Torlon coated with Polyimide	2.7×10^{-7}

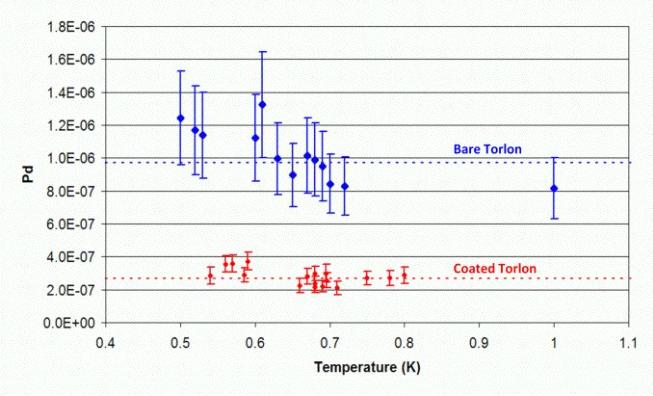

Figure 8: Depolarization probability per bounce vs. temperature for bare Torlon, and Torlon coated with polyimide.

3.4 Guide Fields

Magnets are required to maintain the Helium-3 polarization as the atoms are moved from the injection volume to the measurement cells, and the geometry in the T-valve region (where the Helium-3 plumbing splits to allow entry into the two cells) is particularly challenging. The neutron spin-holding coil magnet design techniques have been applied to the Helium-3 transfer magnets in the "T-valve" region, and the same fabrication technique has been proposed. The physical boundary condition was defined to be a sleeve, mounted onto the Helium-3 plumbing in a series of half-cylinders (Figure 10). Such a geometry greatly simplifies assembly and repair scenarios. The magnetic boundary condition was defined as B_x(inside) = 30 mG and B(outside) = 0 (Figure 9).

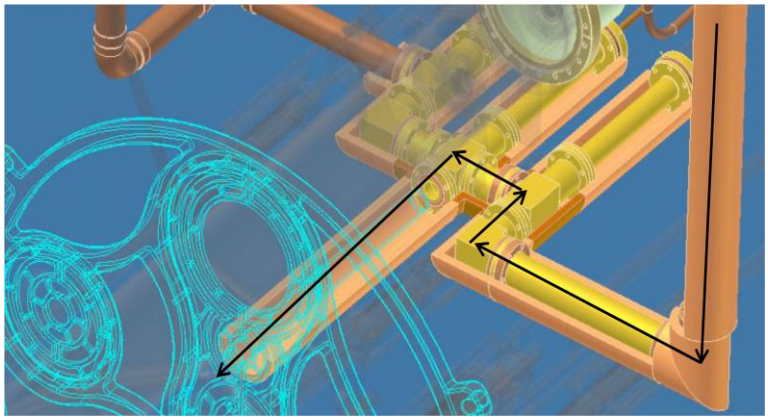

Figure 10: Helium-3 plumbing in the "T-valve" region. The Helium-3 trajectory (through the yellow Torlon plumbing) is shown by the arrows. The transfer magnets are the tan cylinders shown in a cut-away view. The central detector system services, which complicate the geometry in this region, can be seen, but are mostly transparent.

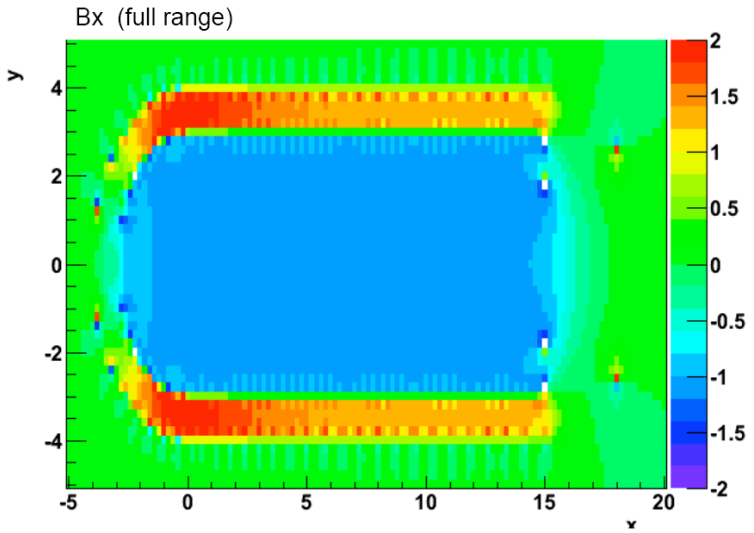

Figure 9: Field map of the elbow region of one of the transfer magnets showing that the current distribution meets the necessary boundary conditions (30 mG inside, 0 outside). Axis units are cm. The color scale units are such that 30 mG = 1.

4 Electric Field

The experimental sensitivity is linearly proportional to the achievable HV breakdown strength, and one of the key advantages of the proposed experimental technique is the large intrinsic breakdown strength of liquid Helium. However, there are a number of challenges associated with generating, maintaining and monitoring the necessary field (sensitivity estimates assume 74 kV/cm across the cell):

1. Effects at the electrode surfaces are likely to limit the maximum sustainable electric field to values significantly below the electric breakdown strength of liquid Helium.
2. A total electric potential of ~600 kV must be generated and applied to the electrodes.
3. The amplification process chosen to generate the operating potential requires disconnecting the HV supply, therefore disabling direct measurement of the electric field.

4.1 Maximum Sustainable Electric Field

Measurements of the maximum sustainable field were made initially with large-scale (~50 cm^2) Aluminum electrodes. These results showed a worrisome reduction in the sustainable field as the temperature was lowered via evaporative cooling [12]. As a result, two separate efforts were started. The first was to develop a small-scale cryostat at Indiana University, that had the advantage of short turn-around times to allow for systematic measurements. The second was to modify the existing large-scale apparatus to allow it to run at the operating temperature.

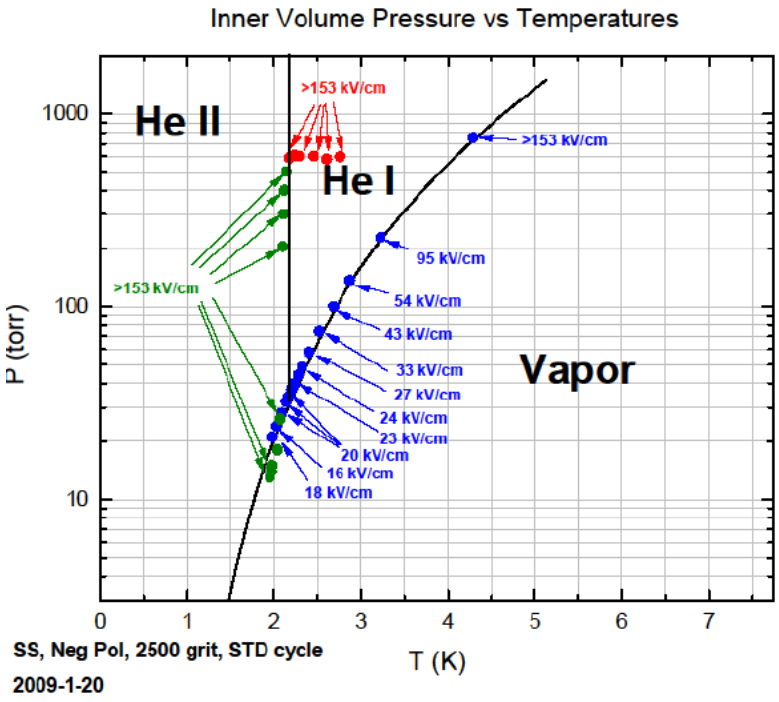

Figure 11: Measured electric breakdown strength in liquid helium at different pressure and temperature with a small mechanically polished electrode. Blue points show sustained fields when cooling along the saturated vapor curve. Red points show sustained fields when cooling isobarically. Green points show sustained fields when cooling through the lambda point isobarically, then reducing the pressure.

Tests in the small cryostat suggested that the observed decrease in the maximum sustainable field was the result of surface effects, likely bubbles:

1. With a small hand-polished electrode, a decrease in the maximum sustainable field was observed as the system cooled along the vapor pressure curve, see Figure 11. Extremely high fields (>153 kV/cm) were achieved below the lambda point with pressurization, albeit still above the nominal operating temperature of 0.45K.
2. Tests with electropolished electrodes achieved breakdown strengths exceeding 344 kV/cm below the lambda point (~2K) without pressurization.

3. During measurements of the scintillation output at low temperature and high fields the system was run for many hours without breakdown at fields of 40 kV/cm and temperatures as low as 0.2K.

Significant cryogenic difficulties were encountered with the large-scale apparatus. At this time the heat load has been greatly reduced, but at 270 mW is still well above the 70 mW required for cooling with existing refrigerators, making it difficult to measure performance improvements for large-scale electrodes with pressurization.

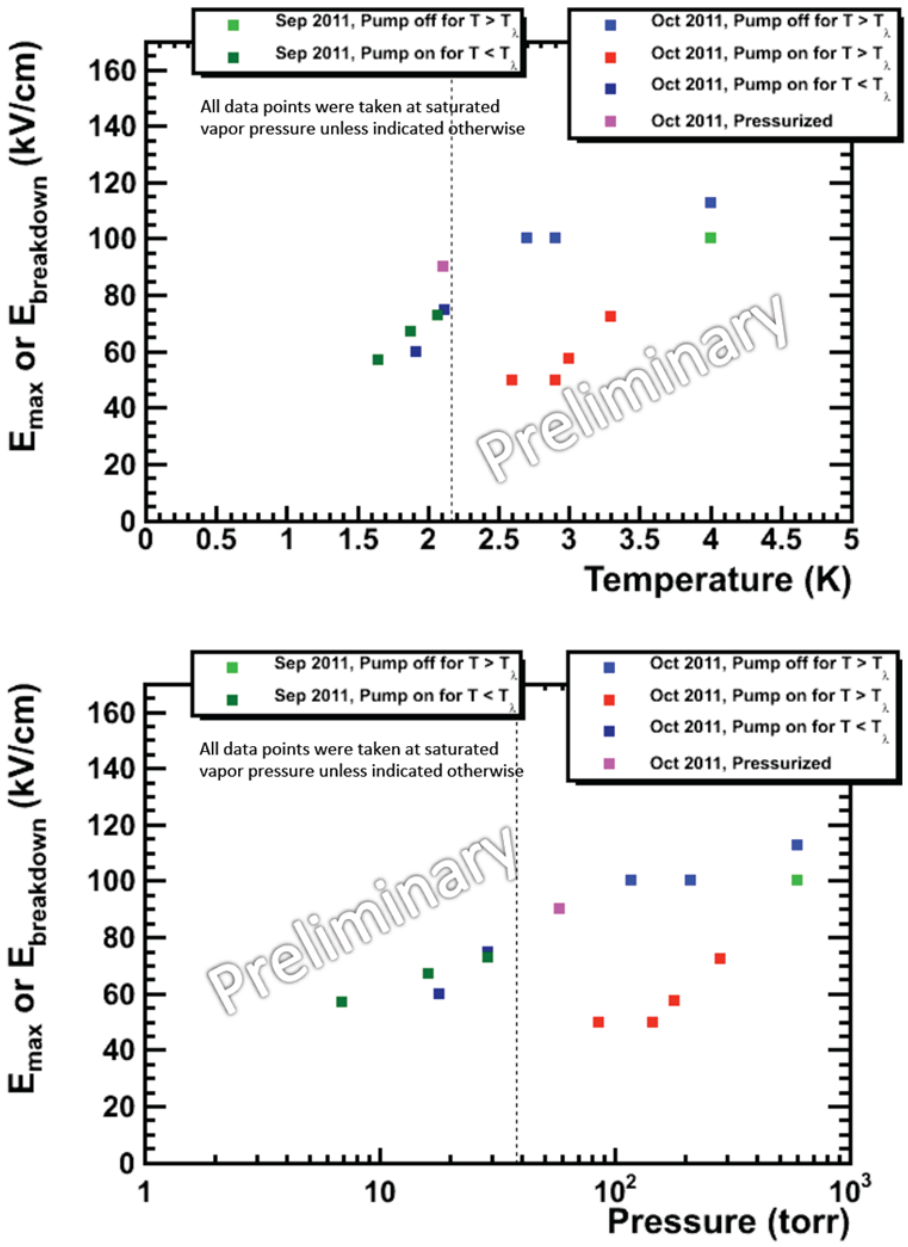

Figure 12: Recent results for maximum sustained electric field, vs. temperature and pressure.

Results (see Figure 12) have recently been collected between 4 and 1.6K at saturated vapor pressure, with and without active pumping on the liquid helium bath. We observed a marked difference in the breakdown field strength between the data taken with and without active pumping on the LHe bath for temperatures above the lambda point. We attribute this to the effect of boiling of the bulk fluid: for normal fluid, if a measurement is taken while the liquid is being pumped, bubbles in the bulk fluid due to boiling of the LHe induce breakdown, lowering the breakdown field strength (see the red points of the new data). When data are taken with the valve to the pump closed, such degradation was not observed (see the blue points of the new data). Superfluid does not boil and there is no difference between the valve open and the valve closed data below the lambda point.

Our interpretation of this data is that degradation of the maximum sustainable field above the lambda point observed previously is due to boiling of the liquid creating bubbles that lead to breakdown.

At T ~ 2.1 K (just below the lambda point), we managed to pressurize the system to ~ 60 torr (the saturated vapor pressure at this temperature is ~30 torr). The breakdown strength was higher for the pressurized case, and consistent with the rest of the data when plotted against pressure. This indicates that the breakdown strength depends on pressure, rather than on the temperature.

The recent results also demonstrated for the first time the ability to sustain the electric field as the electrodes are separated to the full 7 cm gap to amplify the potential – while below the superfluid transition.

The electrodes will be made of acrylic in order to match the thermal coefficient of expansion of the measurement cells and light guides, and will need to be coated with a suitable material (surface resistivity $10 < \sigma\ (\Omega/\text{sq}) < 10^5$, non-magnetic, low neutron activation cross section, durable). Since surface effects are clearly important, it is crucial to test the maximum sustainable electric field using electrodes coated with candidate materials. Resistivity and durability have been measured for several candidate electrode materials (graphite paints, indium-tin-oxide, and titanium nitride). Several candidates have passed these initial tests.

4.2 HV Amplification

Rather than attempt to develop a 600 kV feedthrough, an amplification system using a variable-gap capacitor was shown to work well. A schematic diagram of the electrode system is shown in Figure 13 [12]. An initial potential, V, is applied to the charger electrode while it is in contact with the HV electrode and the gap between the

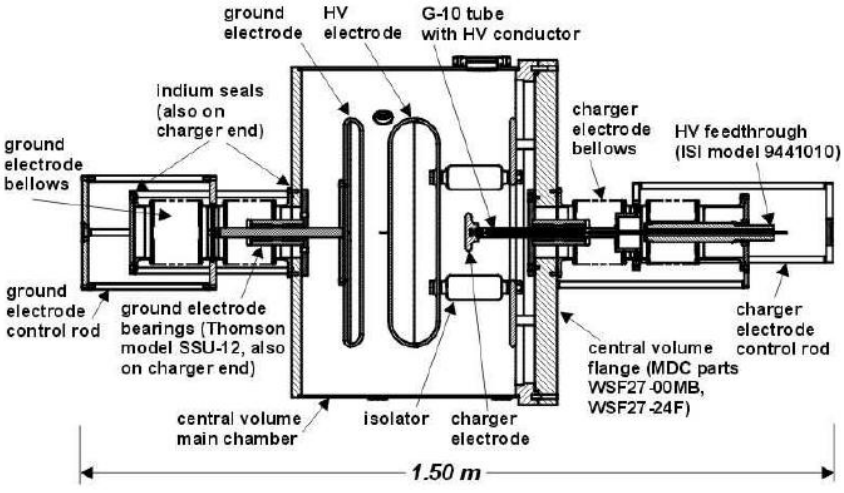

Figure 13: Assembly drawing (elevation, to scale) of HV test system central volume.

ground and HV electrodes is small (few mm). The charger electrode is then disconnected from the HV electrode and the ground electrode is retracted several centimeters from the HV electrode. The decreased capacitance results in an amplification of the potential.

4.3 HV Monitoring (Kerr, E-dependence)

A few percent determination of the electric field is required to ensure sufficient accuracy in the field-reversal to reduce the quadratic v×E systematic error [13].

The ellipticity of linearly polarized light increases when passed through material subjected to an electric field (the Kerr effect). We have measured the Kerr constant in superfluid Helium [14]; at the operating voltage the induced ellipticity is 10-100 μrad, giving a required measurement precision of ~ 1 μrad.

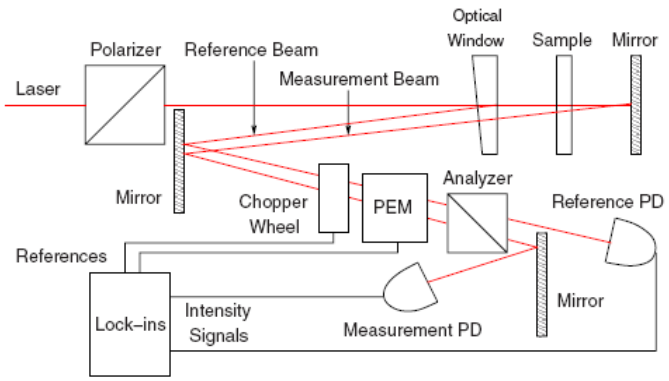

Figure 14: Schematic diagram of optical cancellation measurement apparatus.

Ellipticity can also be caused by birefringence induced by mechanical and/or thermal stress in the measurement cell walls. Half-inch thick slabs of stock acrylic has been found to have ellipticities of ~100 mrad. Annealing reduces this to 7 mrad. An optical cancellation technique has been developed [15] that further reduces this by two orders of magnitude (70 μrad), see Figure 14, and subtraction of the ellipticity offset at E=0 leaves only the fluctuations (1%) on this offset at an acceptable level (0.7 μrad). Birefringence-free acrylic samples are being fabricated to determine whether they can provide further improvements.

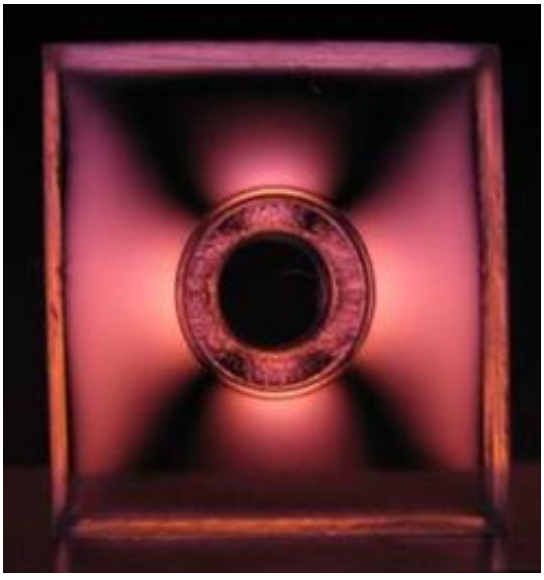

Figure 15: A photograph of a mock-up of the Kerr HV monitor window, viewed through a pair of crossed polarizers. Stress, corresponding to significant ellipticity, is revealed by the colored regions.

Ellipticity will also be induced due to the Kerr effect in the acrylic; at the nominal cell wall thickness the induced ellipticity will be two orders of magnitude greater than the Kerr effect in the Helium. With the optical cancellation technique the 0.1% precision requirement leads to a similar cell wall thickness variation requirement across the physical separation of the two laser beams. Thinning the cell wall eases this requirement proportionally. The thinning process could, in principle, result in significant thermally induced stress and resulting birefringence. To test this, thinned acrylic samples were prepared (glued to a thick, mock cell wall and annealed.

Figure 15 shows a photograph of such a window viewed through a set of crossed polarizers – colored regions have relatively large ellipticity. Significantly less ellipticity is observed in the thinned section; black sections have an ellipticity of less than a few degrees.

Figure 16 shows ellipticity vs. temperature at the center of the thinned region, which performs better than the goal (less than a few degrees change between room temperature and operating temperature). Note: the ellipticity is expected to reach an asymptotic value at ~100 K, since there is relatively little thermal contraction below that temperature.

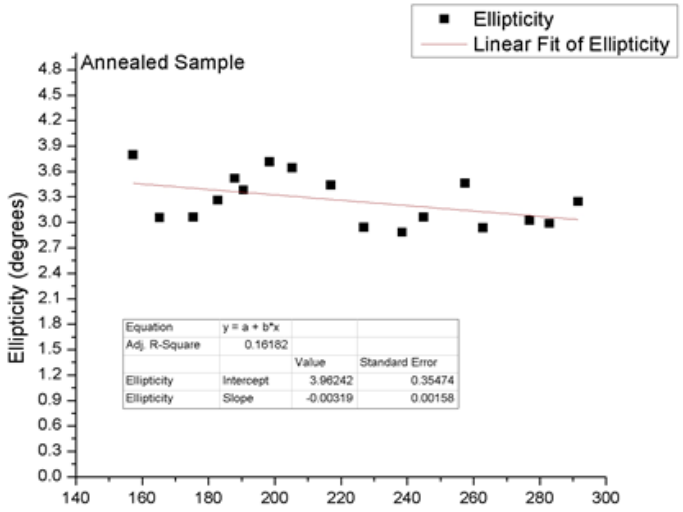

Figure 16: Measured ellipticity at the center of the thinned acrylic sample vs. temperature.

As an alternative (or in addition to) the Kerr-effect, the electric field dependence of the LHe scintillation intensity can be used to monitor the high-voltage. Our measurement of scintillation signal size vs. electric field showed that the intensity of the prompt pulse of α-particle induced LHe scintillation falls with the electric field (Section 6.1). As a result, a 0.5% determination of the scintillation intensity of the n-3He capture events provides the needed 3% determination of the electric field. To do this we need to monitor and control the PMT gain and light collection efficiency to 0.5%. The prototype battery-powered, optically isolated HV power supply has demonstrated this performance (Section 7.2). In addition, the stability of the light collection efficiency can be monitored by painting a small area (few mm diameter) on the sidewalls of the measurement cells with a mixture of scintillator paint and radioactive source. Tests are underway towards the goal of demonstrating that such a scheme will work.

5 Magnetic Field

The neutron magnetic dipole moment is so much larger than the electric dipole moment that the magnetic field environment of the measurement cell is absolutely critical [16]:

- External magnetic fields must be strongly shielded.
- An extremely uniform must be created *in situ*.

In addition, the RF fields for the spin-dressing measurement technique must not generate excessive eddy current heating and the external magnetic shields must allow relatively easy access to the apparatus.

5.1 Magnetic Shielding

The first line of defense for the magnetic shielding is the multi-layer room temperature shielding. The outermost layers are made from μ-metal. The inner-most layer is made from MetGlas. MetGlas comes in ribbons that must be wrapped onto a form. Wrapping techniques were explored and it was discovered that a hybrid winding protocol provides substantially improved axial shielding factors [17], see Figure 17.

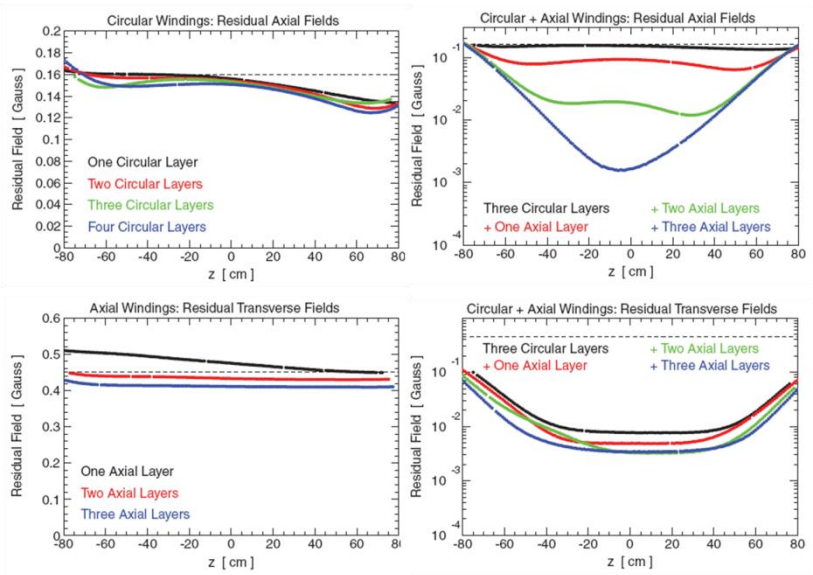

Figure 17: (Upper left) Circular windings alone do a poor job shielding axial fields. (Lower left) Axial windings alone do a poor job shielding transverse fields. A technique that combines both types of windings shield both axial (Upper right) and transverse (Lower right) fields.

The axial shielding factor (~2,000, as calculated in TOSCA) provided by the external multi-layer shield is somewhat low. To improve this, an external system of four rectangular coils, surrounding the multi-layer μ-metal shield was proposed (Figure 18). The concept of these axial shielding compensation coils is as follows: (1) With the Pb superconducting shield above its critical temperature T_c, the currents in the coils are adjusted so that the residual axial shields are minimal; (2) The Pb superconducting shield is

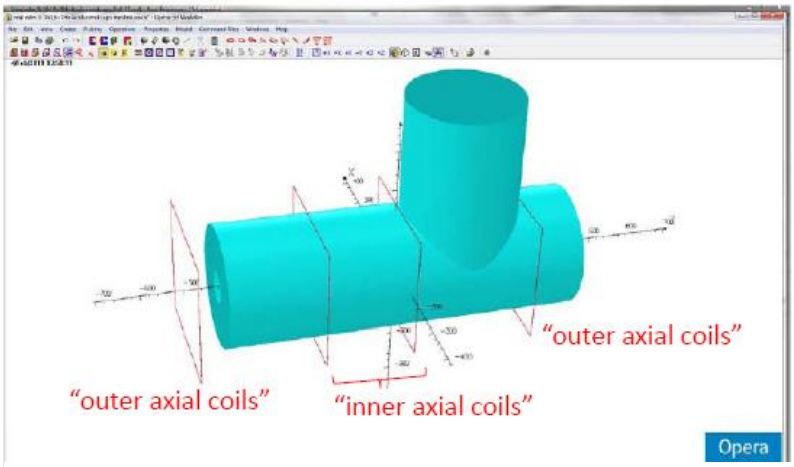

Figure 18: TOSCA model of the axial shielding compensation coils.

Figure 19: Prototype axial magnetic shielding system.

Results from measurements of the residual shielded fields for optimized coil current settings are plotted in Figure 20. The green curve shows the residual axial fields with the coils off, the blue curve shows the fields with the two inner-most coils energized, and the red curve shows the fields with all four of the coils energized at their optimized settings. The data clearly show that the residual axial fields can be reduced to small levels, and that the residual field uniformity can be significantly improved with the use of the external bucking coils.

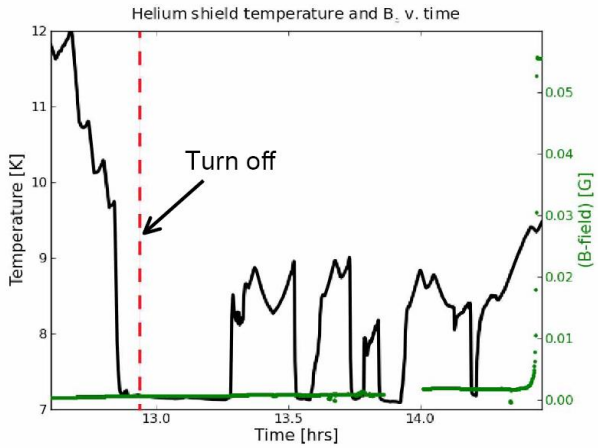

Figure 21: Temperature of the helium shield (left axis) and the axial magnetic field strength (right axis) in the ½-scale magnetic coil package during test of superconducting lead shield. See text for details.

cooled below T_c, thereby locking the (now minimal) axial flux; (3) With the flux locked, the currents in the coils are turned off, to minimize magnetic noise.

A prototype axial magnetic shielding system, consisting of a μ-metal shield (diameter 30", length 72") and four rectangular bucking coils (96" x 96"), has been tested (Figure 19). The two inner-most coils are spaced at the square Helmholtz condition.

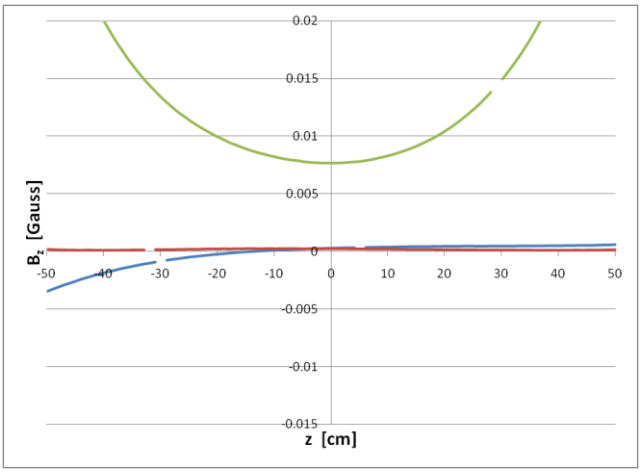

Figure 20: Results from measurements of the residual shielded fields. See text for details.

Combined operation of the external bucking coils with the superconducting shield has been experimentally tested (Figure 21) using the ½-scale magnet package prototype (discussed in the next section). In this test a set of bucking coils (similar to the ones described above) was used to cancel external magnetic fields at a time earlier than shown in the figure. Shortly before the red dashed line the lead shield went through the superconducting transition. Due to the Meissner effect, the superconductor, successfully repelled the external fields, as seen when the bucking coils were switched off (indicated by the red dashed line). The transition back to the normal conducting state can be seen at the far right of the plot where the field rapidly rises to the unbucked external field value.

5.2 Field Uniformity

Field uniformity is crucial for reducing the geometric phase systematic error, and for maximizing the neutron and Helium-3 polarization lifetimes.

Tests with a 1/6th-scale coil allowed for optimization of the coil designs and demonstrated the beneficial effects on field uniformity due to the combined operation of the superconducting lead shield and cryogenic ferromagnetic shield (whose boundary conditions allow a more uniform magnetic field to be obtained at the measurement cells), see Figure 23.

Room temperature measurements of the field uniformity of the ½-scale coil package (Figure 24) have been made at 891 and 200 mG [18]. Cryogenic measurements (95 K) were made at 240 mG. Results, scaled to the full-size coil, are shown in Figure 22. Observed gradients meet, or nearly meet, required levels, assuming they scale with B_0.

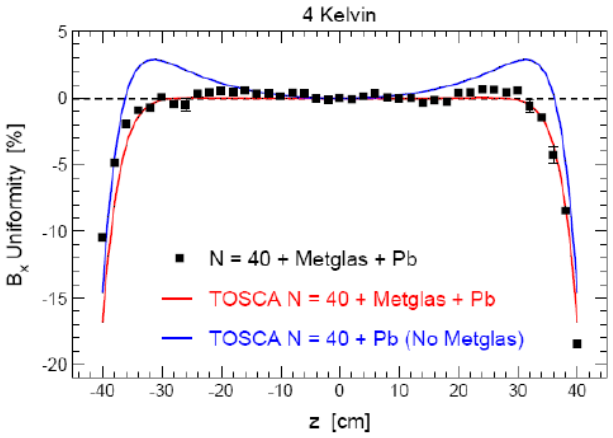

Figure 23: Field uniformity in the B0 field direction with and without the cryogenic ferromagnetic shield. Results with the ferromagnetic are compared to the calculated field uniformity for the 1/6th scale prototype.

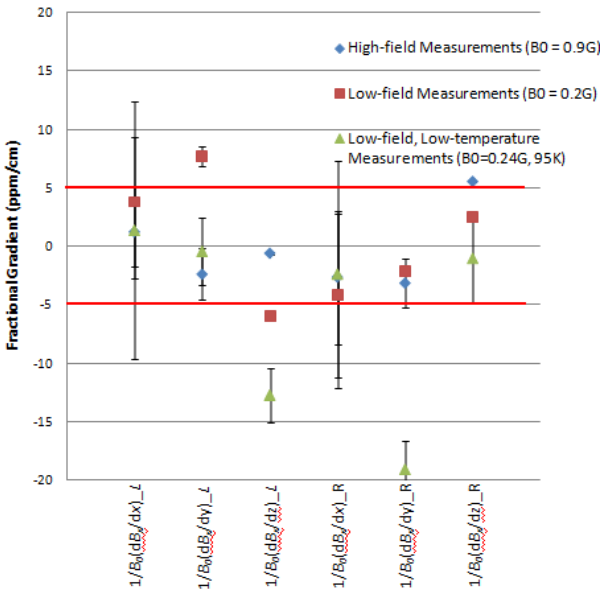

Figure 22: Fractional gradients measured in the 1/2-scale test cryostat under a variety of conditions.

Figure 24: (Left) The ½-scale bare coil being moved. (Right) The ½ scale magnet test cryostat with the B_0 magnet inside and the vertical magnet mapper installed.

5.3 Eddy Current Heating

A prototype pair of dressing coils, an inner coil to apply the dressing field to the measurement cells, and an outer coil to actively shield components outside the magnet coil package, was successfully tested. Figure 25 shows a x100 reduction in the dressing field at a position outside the two dressing coils corresponding to the cryogenic ferromagnetic shield at an optimized ratio of currents in the inner and outer dressing coils..

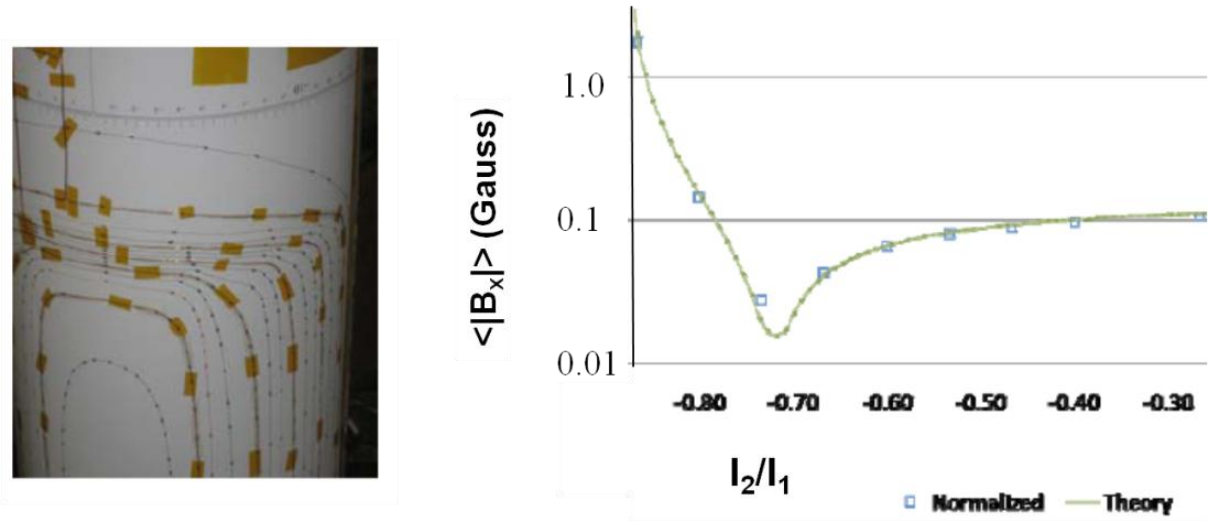

Figure 25: Outer dressing coil prototype (left) and comparison to theory (right).

5.4 Access to Magnetic Shielding Interior

We estimate that the room-temperature shield end caps will need to be removed dozens of times during experiment commissioning and operation to access the interior of the experimental apparatus. This operation needs to be easy and quick, while still providing a good magnetic seal. The standard magnetic connection technique involves overlapping flanges compressed together with a high density of screw/nut connectors, which on the scale of the nEDM shields would be difficult, time consuming, and prone to damaging the sensitive μ-metal material.

An alternative technique was evaluated, in which μ-metal foils were configure to overlap the seams of a prototype end cap, and clamped in place with hose clamps (Figure 26). The shielding was found to be as good, or better than, the standard technique, see Figure 27.

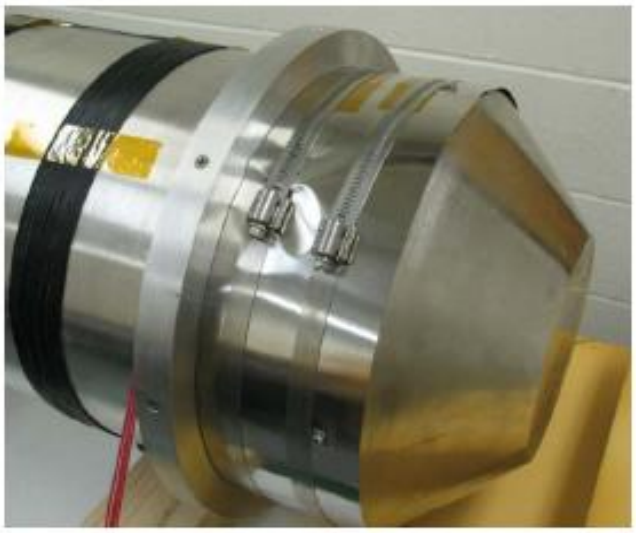

Figure 26: Photograph of clamped μ-metal foil endcap seal.

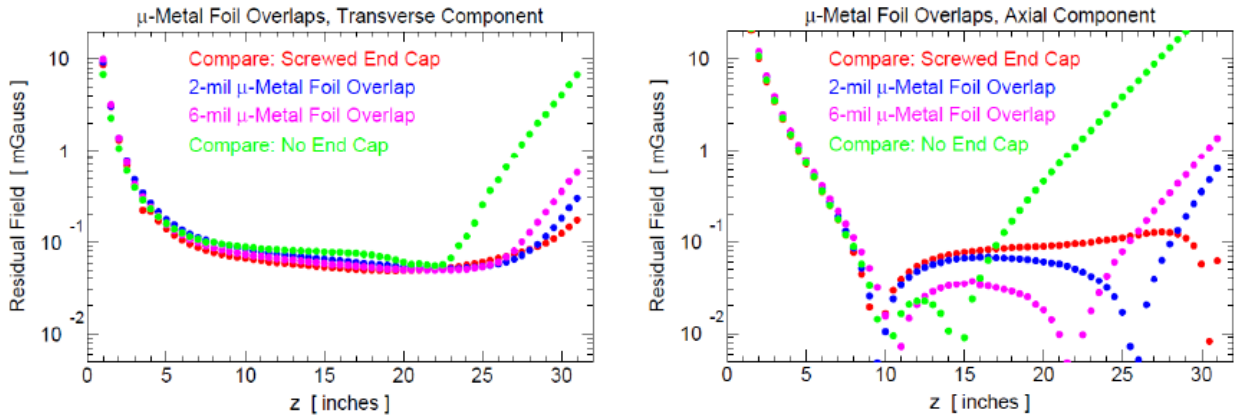

Figure 27: Residual transverse (left) and axial (right) fields vs. longitudinal position for different endcap configurations: red) screwed endcap, blue) 2 mil μ-metal foil, magenta) 6 mil μ-metal foil, green) no endcap.

6 Neutron-capture Signal

The signal for a neutron capture event is the detection of scintillation light generated by the capture of UCNs by Helium-3. As detailed in Table 2, there are a large number of places for the signal to be degraded, and the initial signal (an estimated 4,800 XUV photons) is expected to result in an average detected signal size of 15.5 photoelectrons. We have measured many of these effects as a part of our R&D program, as described in the following subsections.

Table 2: Estimate of the number of PE's based on values from the literature and from measurements by the nEDM collaboration.

Factor	Value	% Error	Note
N_{XUV}	4800	15	# XUV photons produced in the capture event at E = 0 kV/cm. *Assuming (pessimistic) that prompt fraction of scintillation for capture products is the same as for α's* [19].
ε_{HV}	0.76	5	Change (loss) in initial scintillation intensity at 74 kV/cm. *nEDM measurement with α's (Figure 28)* [20].
$\Omega_{TPB}/4\pi$	0.896	1	Solid angle of TPB coverage in cell side walls. *Calculation.*
ε_{conv}	0.33	19	XUV → blue photon conversion efficiency in dTPB/PS. *Extrapolation to 85 nm from 120 nm measurement by CLEAN/DEEP* [21].
$\varepsilon_{collect}$	0.214	5	Fraction of converted blue photons trapped in cell wall. *Calculation based on PMMA index of refraction + nEDM measured mirror reflectivity (Figure 29)* [22].
ε_{coated}	.916	5	Efficiency to transmit light down cell wall. Losses due to optical properties of WLS coating. *nEDM measurement (Figure 30)* [22].
$\varepsilon_{endcaps}$	0.87	1	Efficiency to transmit light down cell wall. Losses due to leakage into font and back cell walls. *Calculation*.
ε_{holes}	0.97	10	Relative efficiency to transmit light down cell wall. Losses due to V1 Valve holes. *Calculation*.
ε_{gaps}	0.78	5	Efficiency to transmit light through two gaps at exit of central volume. *Calculation*.
g_{AR}	1.05	4	Gain in transmission efficiency through the gaps due to use of anti-reflective coating. *nEDM measurement.*
$\varepsilon_{straight\text{-}guide}$	0.64	3	Efficiency to transmit light down straight lightguides of the necessary length. *nEDM measurement (Figure 31)* [22].
ε_{bend}	0.88	10	Relative efficiency to transmit light down bent guides of the necessary length. *Calculation plus initial nEDM measurement.*
ε_{PMT}	0.18	10	Quantum efficiency of cold (4K) PMT (Hamamatsu 7725). *nEDM measurement (Figure 33)* [23] *+ manufacturer specification @ room temperature.*
#PE	**14.8**	**32**	**The product of all the above parameters; errors added in quadrature**

6.1 Scintillation Light vs. HV (ε_{HV})

An experiment was carried out to determine the effect of strong electric fields and temperature on the magnitude of the scintillation signal generated by an alpha source. As shown in Figure 28, there is relatively little effect from temperature, but some decrease in the signal size as the electric field increases. It is worth noting that the signal size (<PE> = 10.4) was in good agreement with the predicted value (<PE> = 9 ± 3) using an analysis similar to that in Table 2.

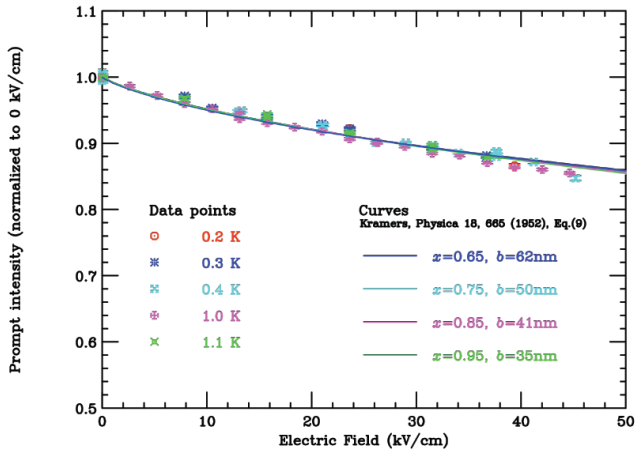

Figure 28: Relative scintillation signal magnitude vs. electric field for different temperatures. Curves are for different parameter choices in the columnar recombination theory used to describe the data [20].

Analysis of the data showed that the observed dependence can be understood using a columnar theory of recombination [20]. Together with a model for quenching of the prompt scintillation a prediction for the number of XUV photons produced in neutron-3He capture events can be made, which suggests a somewhat increased signal size - ~25% larger than currently estimated [20].

6.2 Lightguide Transmission ($\varepsilon_{collect}$, ε_{coated}, g_{AR} $\varepsilon_{straight\text{-}guide}$, ε_{bend})

The XUV scintillation light is converted to blue light with a wavelength-shifting layer coated onto the cell side walls. Light emitted at angles less than the critical angle and in the direction of the PMT are trapped within the guide. A fraction of the light emitted in the direction opposite the PMT will be reflected and also trapped within the guide [22], see Figure 29.

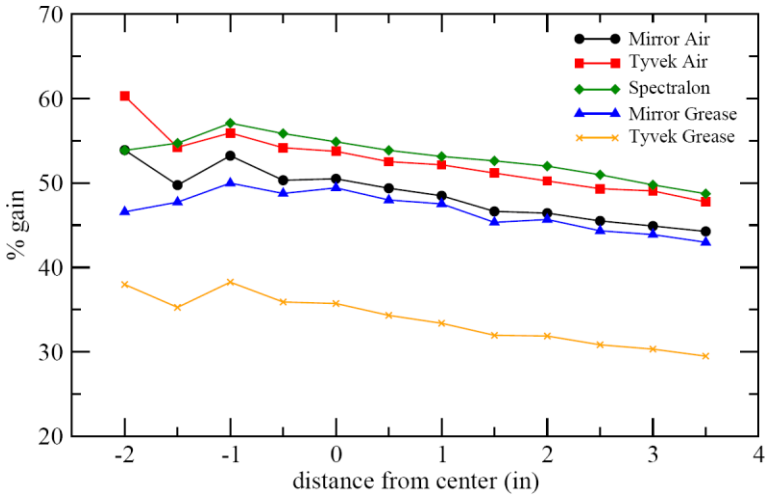

Figure 29: Reflectivity of different mirror materials and mirror/lightguide interface.

Not all of the trapped light will be successfully transmitted down the measurement cell wall to the start of the light-guides. This was measured for acrylic plates coated with TPB/PS [22], see Figure 30.

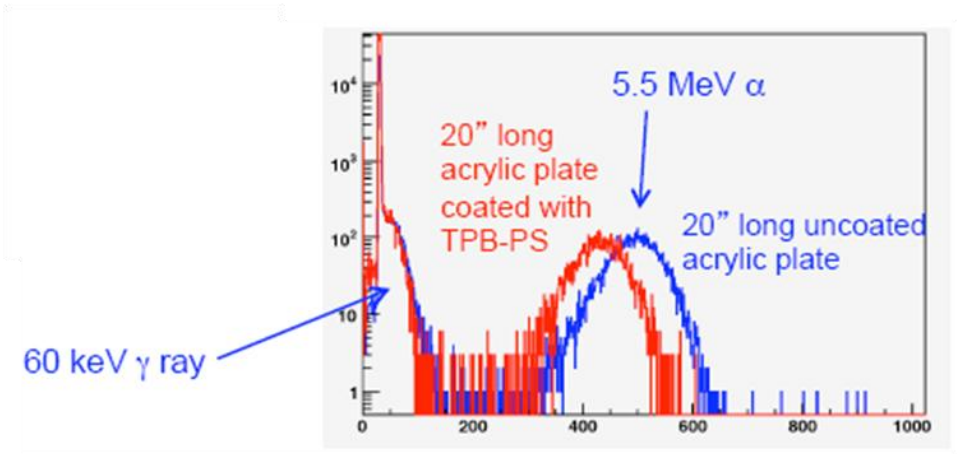

Figure 30: Difference in light transmission down an uncoated acrylic plate (blue) and a plate coated with TPB/PS (red).

In exiting the central volume the light must pass through two gaps (to minimize heat loads and to prevent problems with differential thermal contraction) on either side of a viewport. The viewport is coated with anti-reflective coating in order to minimize losses. The resulting photoelectron signal was increased by 5%, consistent with expectations.

The light guides (60" long) are made of ½"-thick UVT acrylic. The attenuation length has been measured to be 142" and 155" for the different strip widths that comprise the complete guide [22], see Figure 31.

The lightguides must be bent, in order to transition from 1 cm × 7 cm (or 10 cm) to a 5 cm diameter circle, and to keep clear of the charging electrode. The fixturing for bending the lightguides is shown in Figure 32. Simulations predict a 15% loss due to the bends. This has been achieved experimentally for individual acrylic strips, but not yet reproducibly.

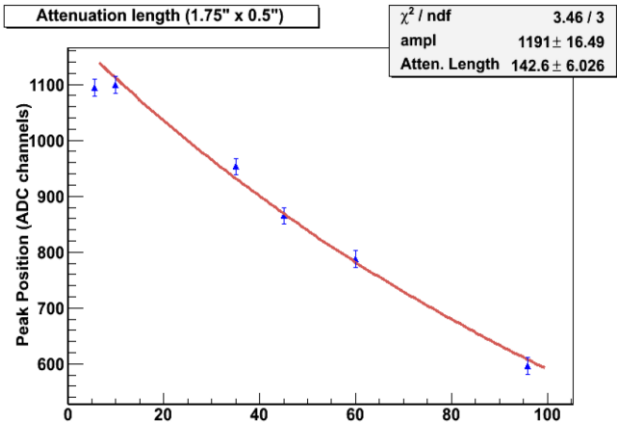

Figure 31: Signal vs. length (in inches) for 1.75" x 0.5" UVT acrylic strips. The attenuation length is found to be 142".

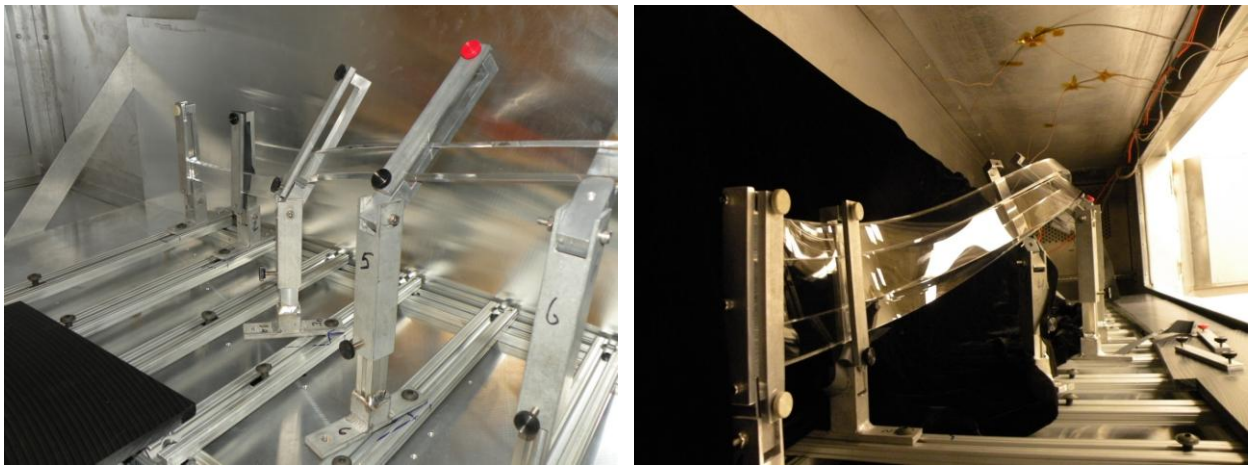

Figure 32: (Left) One of three acrylic strips that make up a full-scale light guide, shown in the fixtures used to bend it into the required complex shape. (Right) Photograph of the full-scale three-strip UVA prototype. The measurement cell end of the guide is in the foreground.

6.3 Cold PMT (ε_{PMT})

Hamamatsu produces a PMT (R7725-mod) modified with a platinum underlayer to allow for cryogenic operation. Measurements of efficiency vs. temperature, relative to the quoted efficiency of an unmodified PMT at room temperature (25%), are shown in Figure 33 [23].

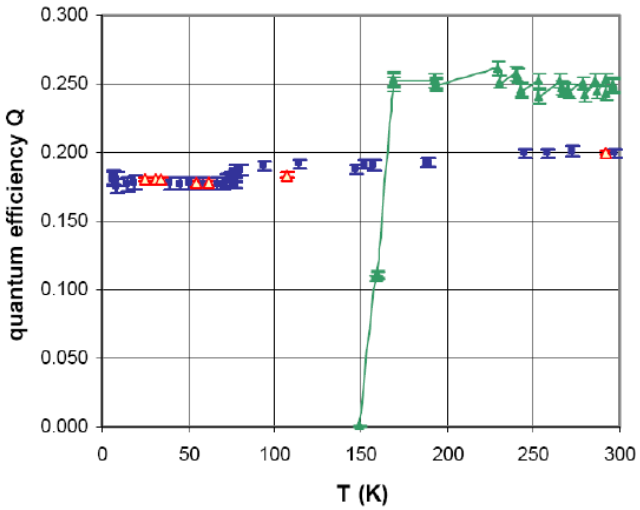

Figure 33: Quantum efficiency vs. temperature for a normal PMT (green), and for a modified tube (blue and red), measured during cool-down and warm-up, respectively).

6.4 Sensitivity to Scintillation Signal Size

To evaluate our sensitivity to the signal size, Figure 34 shows the photoelectron distributions for simulated signal and background sources for different assumed values of the mean number of photoelectrons for the neutron capture signal. We can efficiently reject backgrounds with two cuts: a timing coincidence between two PMTs is required and an energy cut, centered on the capture signal peak, is enforced. Table 3 shows the effect on detection efficiency and on rejection of β-decay background (the primary background source). With these two cuts (energy cut values are shown in table) there is little change for $\langle PE \rangle \geq 6$.

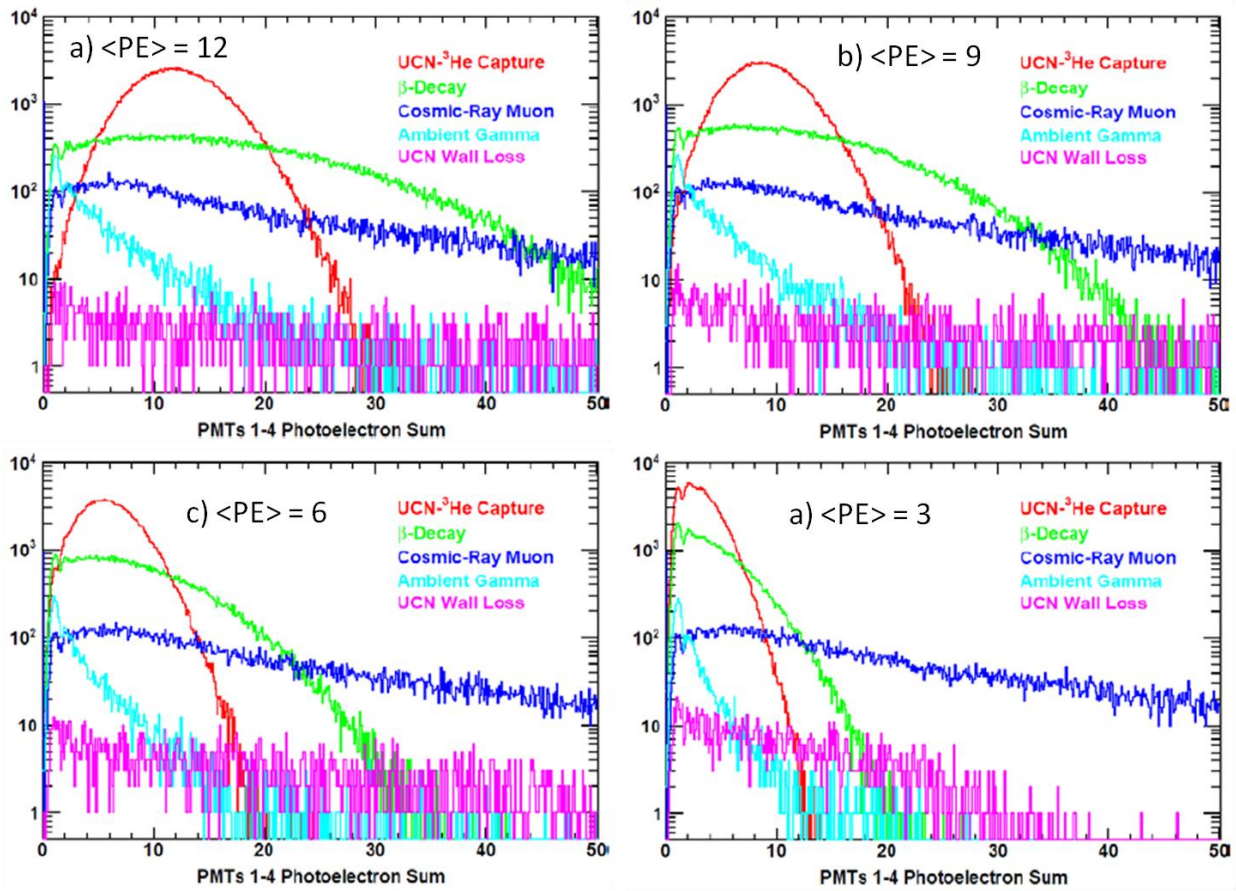

Figure 34: Photoelectron spectrum for signal and background sources for different assumed values of the mean number of photoelectrons for the neutron capture signal.

Table 3: Change in signal efficiency and β-decay background rejection for different values of the photoelectron peak for signal events.

<PE>	Energy Cut (PE min, max)	ε_{signal}	f_{β}
12	(6,18)	0.88	0.57
9	(4,14)	0.87	0.53
6	(2,10)	0.85	0.48
3	(2,7)	0.59	0.52

7 Helium-3 Precession Signal

The experiment uses two complementary methods to extract the value of the neutron electric dipole moment: the free-precession method, in which SQUID magnetometers are used to measure the Helium-3 precession frequency, which is then added to the beat frequency measured via scintillation light to get the neutron precession frequency, and the spin-dressing method, in which an RF magnetic field is used to equalize the gyromagnetic ratios of the Helium-3 and the neutrons.

In the free-precession method, the SQUIDs must meet challenging requirements:

- Sensitivity must be sufficient to detect the signal with a precision much better than the measurement precision of the beat frequency - despite the low Helium-3 concentration and the "wrong" orientation of the SQUIDs relative to the Helium-3 spins necessitated by the experiment geometry.
- Noise (due to nearby electronics and vibrations) must be similarly small.

Spin-dressing of Helium atoms had not previously been demonstrated.

7.1 SQUID Sensitivity

The precession of Helium-3 spins was detected with ultra-low field NMR [24]. Sensitivity, extrapolated to the nEDM geometry, was more than sufficient (δf_3 ~ 1.2 μHz/cycle, compared to δf_{beat} ~ 26 μHz/cycle).

7.2 SQUID Noise

SQUID noise must be less than 0.5 fT/√Hz. Such levels have been achieved in a "real-world" environment (airport cargo monitoring) by a group at Los Alamos [25]. Such levels should be achievable if the SQUIDs operate inside a Faraday cage, and all electrical equipment inside the Faraday cage is either disconnected during the measurement cycle or battery-powered; a significant effort has been made to demonstrate this.

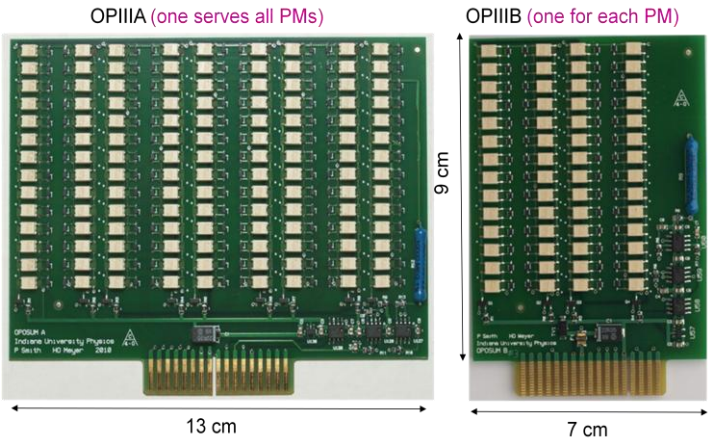

Figure 35: Photographs of printed circuit boards for DC-powered, optically-isolated PMT HV supply.

The cryovessel serves as the Faraday cage for the SQUIDs. There are a fair number of penetrations of this cage, but solutions have been identified to block them.

Most of the electrical equipment can either be physically disconnected or battery powered. The most challenging exception was felt to be the high-voltage supply for the PMTs. A DC-powered, optically isolated, PMT HV supply (Figure 35) was designed, built and demonstrated to satisfy all requirements [26]. Output potential stability of better than 0.05% vs. nominal ranges of input voltage, load

current and temperature was observed; gain stability of better than 0.5% is inferred for hit rates far in excess of what is expected.

A surplus, multi-layer magnetically shielded room was obtained and re-constructed to serve as a facility to test SQUID compatibility with other electrical equipment, Faraday-cage sealing techniques, and charging and regulator systems.

Figure 36: Magnetic shield room under construction.

7.3 Spin-Dressing

Spin-dressing refers to the modification of the precession frequencies of the stored UCN and Helium-3 when an RF field is applied transverse to the direction of the uniform magnetic field. At the "critical" dressing field, the precession frequencies are equalized, allowing optimal utilization of Helium-3 as a co-magnetometer for the nEDM experiment. A measurement using the polarized atomic Helium-3 source at LANL successfully observed the dressed-spin effect and demonstrated the theoretically expected behavior [28], see Figure 37.

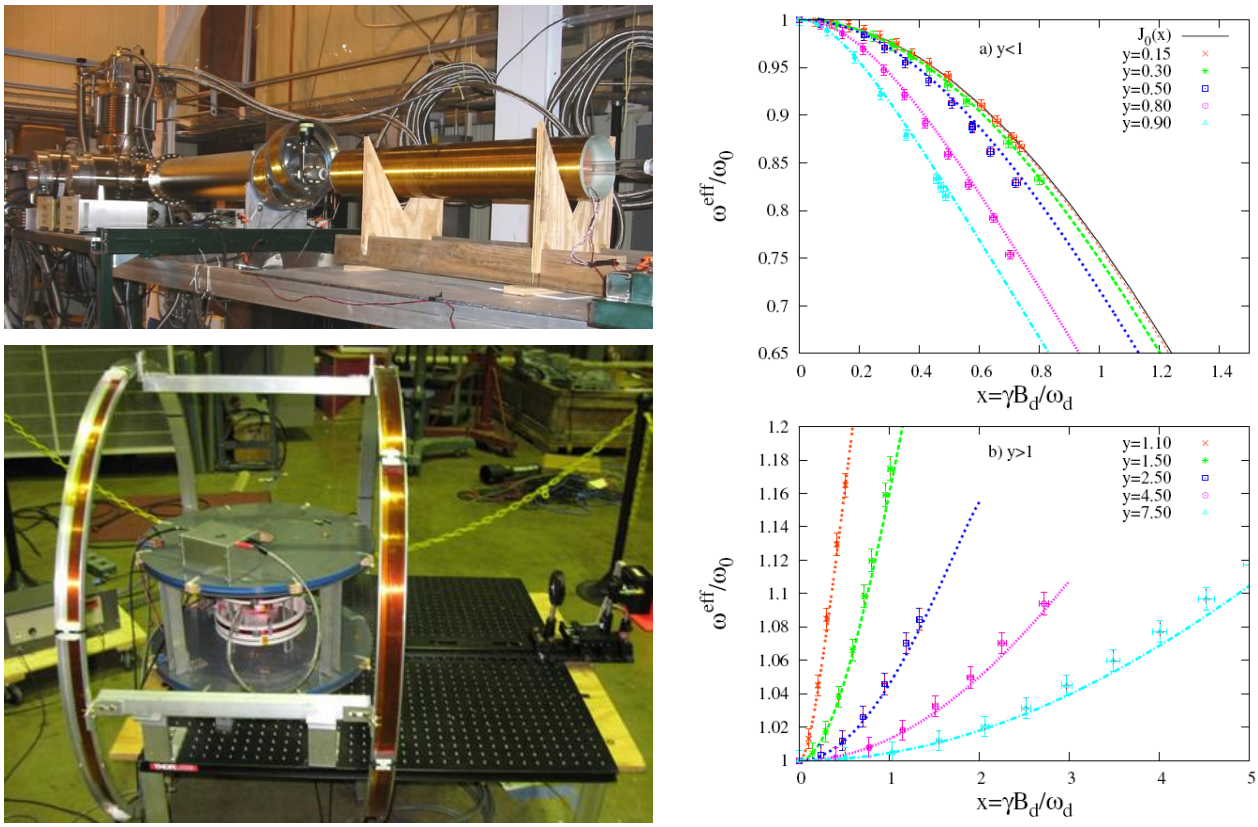

Figure 37: Experimental setups used to measure the spin-dressing effect in Helium-3 at LANL (top) and UIUC (bottom). Results from the UIUC measurement compared to theoretical calculations [29].

Another measurement, shown in Figure 37, was performed at UIUC using polarized Helium-3 stored in an acrylic cell. The Helium-3 atoms were polarized using the metastability spin-exchange technique, and the modification of the precession frequencies was observed over a broad range of the amplitude and frequencies of the dressing field [29].

8 Mechanical Issues

8.1 Valves

nEDM makes use of a number of valves to control the flow of polarized and unpolarized ^{3}He and to regulate the pressure of LHe in parts of the system from essentially 0 to 1 atm. The most challenging valves must be of large aperture (2.5 cm diameter), made from "Helium-3 friendly" materials, thermally isolating, and able to hold off 1 atm of superfluid LHe. A full-size prototype valve was constructed using a “cork-in-bottle” seat/boot design, an off-the-shelf Be-Cu bellows, a double seal (closed and open) to protect Helium-3 from the bellows, two sliding “linear bearings” maintain alignment of seat/boot and a Torlon 4203 body. This valve, see Figure 38, was cycled successfully more than 10,000 times.

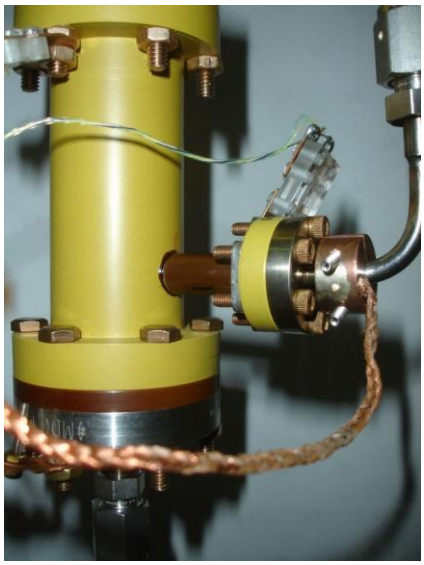

Figure 38: Picture of prototype Helium-3 valve.

8.2 Thermal Contraction

The experimental apparatus must accommodate significant thermal contraction of connections between the Helium-3 services modules and the central detector system – a problem made more challenging by the fact that metal components are generally not allowed. Several attempts to make non-metallic bellows have met with partial success. In the latest attempt, Kapton was deposited on an aluminum mandrill. However, when the mandrill and resin were heated to cure the Kapton, bubbles formed in the thicker parts of the coating on the inner corrugations of the bellows (see Figure 39). This problem appears to come from the long time that is required to bring the large thermal mass of the mandrill to the cure temperature. In a new approach, we are coating a much thinner (0.004" thick) (and presumably more easily heated) beryllium-copper (BeCu) bellows with Kapton. We then plan to remove the BeCu material using a ferric-chloride solution, the same solution that is typically used to etch away copper from printed circuit boards.

Figure 39: Initial attempt at forming a Kapton bellows.

8.3 Cryogenic Seals

Several different seals needed for the Helium-3 plumbing were cryogenically tested and found to be superfluid tight: Torlon mating "V-groove" seals (rotating and non-rotating), and seals for non-metallic flanges that require the use of blind tapped holes. See Figure 40.

A test-bed for evaluating the sealing techniques for the large diameter non-metallic flanges on the central volume endcaps at sub-4K temperatures has recently been assembled at NCSU. A 10" diameter G-10 flange with an 8" ID, 0.1" wide, 0.005" thick Kapton seal has been measured to be leak tight at 10^{-9} at room temperature using glass-filled plastic bolts to compress the flange. Diffusion tests are underway.

Figure 40: Photograph of the Torlon flange concept test fixture. Two types of seals (one with blind tapped holes, and one with rotatable seals) are tested simultaneously.

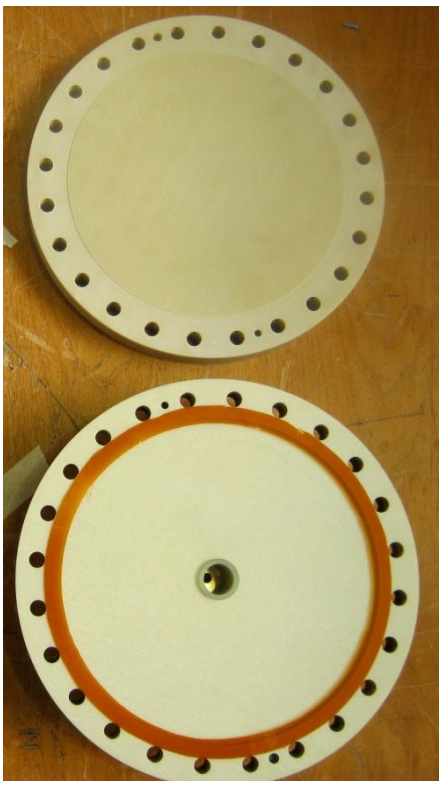

Figure 41: (Left) Photograph of the cryostat for testing large non-metallic flange sealing techniques. (Right) Photograph of 10" G-10 flange prior to assembly. The Kapton O-ring that provides the seal can be seen on the bottom half of the flange.

9 Geometric Phase Measurements

The geometric phase is the most important known systematic effect for the nEDM experiment. This effect, caused by the interaction between the relativistic v×E magnetic field of both neutrons and Helium-3 atoms, with gradients in the applied magnetic field, results in a frequency shift that varies linearly with the electric field – a false EDM [27]. The size of the false EDM depends on the size of the field gradients and on the operating temperature, but is likely to be roughly the same size as the goal statistical sensitivity. Therefore, it will be important to have a good understanding of its actual value under our experimental conditions. As we understand the expected field and temperature dependence of the effect, we can adjust those parameters, quantify the change in the measured EDM and verify that the expected behavior is observed, and subtract the false EDM from our measured EDM signal with a small relative uncertainty.

We have shown how to extend the theoretical framework for calculating the geometric phase beyond the short mean-free-path limit (where diffusion applies and wall interactions are relatively unimportant) and beyond the assumption of linear gradients so that the effect can be calculated with the actual measured magnetic field distribution and (hopefully) the effects of magnetic impurities on the measurement cell wall can be evaluated [30].

An experimental apparatus that measures the position-position correlation functions by measuring the T1 relaxation in known gradients has been constructed. Preliminary data at low Helium-3 concentrations (in order to increase the mean-free-path to the point where wall interactions become important) has been collected and is being analyzed.

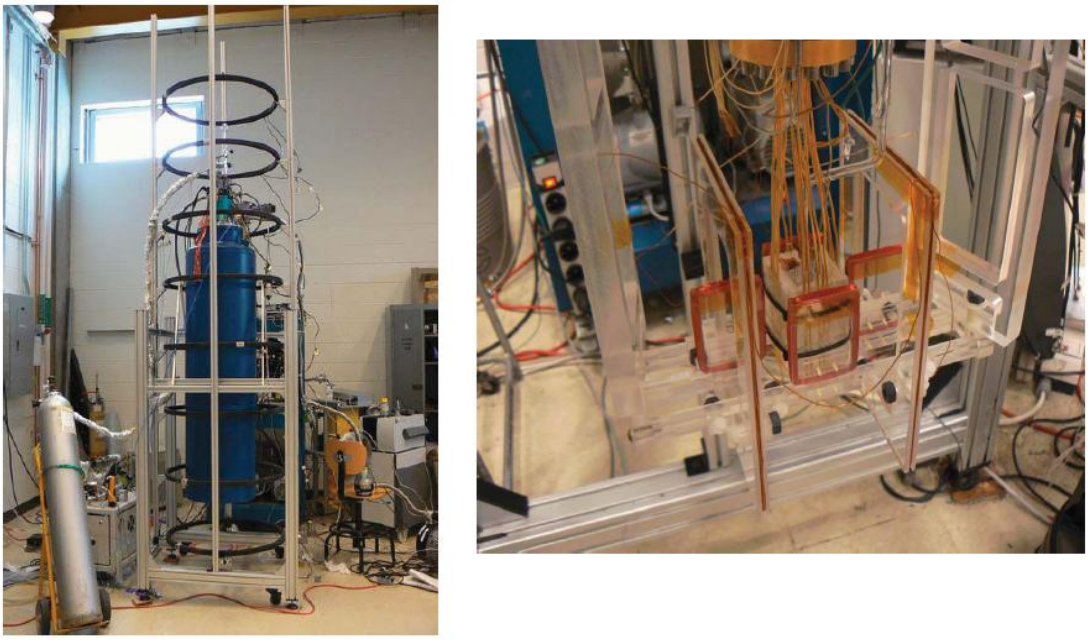

Figure 42: Apparatus used to measure the Helium-3 position-position correlation function through gradient-induced longitudinal relaxation (T1) of spin-polarized helium-3. (Left) Cryostat inside external field coils. (Right) Acrylic measurement cell and gradient/pickup coils removed from the cryostat.

10 Measurement Cycle Simulations

A GEANT-4 based framework has been established to allow simulation of the measurement cycle. Inputs include UCN density, storage time, polarization and polarization lifetime, Helium-3 density, polarization and polarization lifetime, E and B-field strengths, flux and energy spectra for different background sources, and fill/measurement times (Table 4).

Table 4: Measurement cycle simulation inputs and notes.

Input	Notes
UCN density	8.9 nm flux from beamline simulations + storage time
UCN storage time	Assumed
UCN polarization	Beamline simulations
UCN polarization lifetime	Projections based on expected field gradients.
Helium-3 density	Optimized based on other parameters
Helium-3 polarization and polarization lifetime	Projections based on measured material properties and expected field gradients.
E-field strength	Chosen
B-field strength	Chosen to balance geometric phase, 3He polarization lifetime.
Cosmic flux/spectrum	PDG
Ambient flux/spectrum	Measurements at FnPB
Activation flux/spectrum	Not included
Fill/measurement times	Optimized based on above in separate calculation

Two 100 million-event datasets were generated and subjected to multiple blind analyses, one with the neutron β-decay electron asymmetry parameter A = -0.1173 (PDG), and one with A = -1, amplified to search for a hypothesized systematic error). Results with the PDG value for A are shown in Figure 43; they are consistent with each other and with the EDM input value. In addition, the statistical accuracy agrees with analytical expectations. No effect is seen with the amplified value of A. A one-billion-event sample has also been generated, but analysis is incomplete.

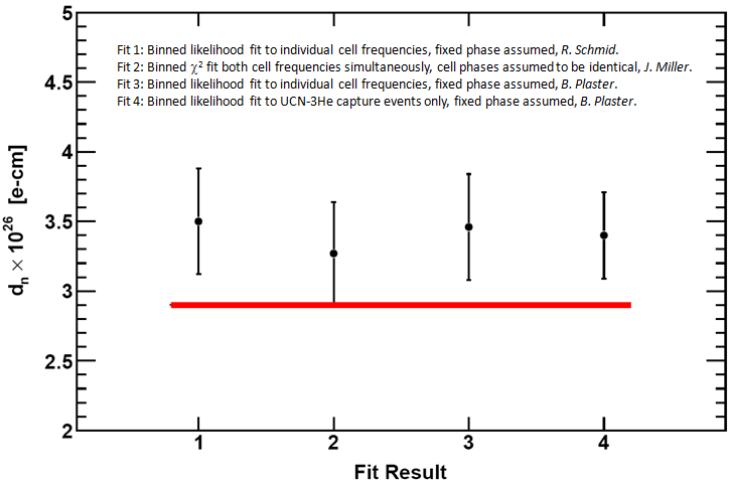

Figure 43: Fit results from different analyses of the 100M dataset. The red line is the input value for the neutron EDM. Fit results 1 and 2 are from independent blind analyses. Fit results 3 and 4 are from an un-blinded analysis. Fit 4 is to a subset of the data that includes only capture events (no background events, and no cuts to remove backgrounds) demonstrating no discernible effects from backgrounds or cuts.

References

[1] R. Golub and S.K. Lamoreaux, Phys. Rep. **237**, 1 (1994).

[2] C. Crawford *et al*., nEDM Internal Report (2011).

[3] V. Cianciolo *et al*., nEDM Internal Report (2011).

[4] W.C. Griffith *et al*., nEDM Internal Report (2011).

[5] C.M. O'Shaughnessy *et al*., Nucl. Instrum. Meth. **A611**, 171 (2009).

[6] J. Torgerson and S.K. Lamoreaux, nEDM Internal Report (2011).

[7] S.K. Lamoreaux *et al*., Europhys. Lett. **58**, 718 (2002).

[8] D. Greywall, Phys. Rev. **B23** (1981) 2152;
M. E. Hayden, S.K. Lamoreaux, and R. Golub, "Evaporative Isotopic Purification of Superfluid Helium-4," in Y. Takano, S.P. Hershfield, S.O. Hill, P.J. Hirschfeld, and A.M. Goldman Eds, "Low Temp. Phys: 24th Intl. Conf. Low Temp. Phys.," AIP Conf. Proc. **850**, 147 (2006).
D. Beck, G. Seidel, S. Williamson, nEDM Internal Report (2010).

[9] D. Kendellen and D. Haase, nEDM Internal Report (2011).

[10] A. Chen, Senior Undergraduate Thesis, UIUC (2011).

[11] Q. Ye *et al*., Phys. Rev. **A77**, 053408 (2008);
Q. Ye *et al*., Phys. Rev. **A80**, 023403 (2009);
Q. Ye, Ph.D. Thesis, Duke University (2008);
J. Yoder, Ph.D. Thesis, UIUC (2010).

[12] J.C. Long *et al*., arXiv:physics/0603231v1 [physics.ins-det] (2006).

[13] S.K. Lamoreaux, Phys. Rev. **A53**, R3705 (1996).

[14] A.O. Sushkov *et al*., Phys. Rev. Lett. **93**, 153003 (2004).

[15] B.K. Park *et al*., Rev. Sci. Instrum. **79**, 013108 (2008).

[16] R. Alarcon *et al*., nEDM Internal Report (2008).

[17] S. Malkowski *et al*., Rev. Sci. Instrum. **82**, 075104 (2011).

[18] A. Perez Galvan *et al*., Nucl. Instrum. Meth. **A660**, 147 (2011).

[19] J.S. Adams *et al*. Phys. Lett. **B341**, 431 (1995).

[20] T. Ito *et al*., arXiv:1110.0570v1 [nucl-ex] (2011).

[21] V. Gehman *et al.*, arXiv:1104.3259v1 [astro-ph.IM] (2011).

[22] A. Kolarkar *et al*., nEDM Internal Report (2011).

[23] H. O. Meyer, Nucl. Instrum. Meth. **A621,** 437 (2010).

[24] I. Savukov *et al*., J. Mag. Reson. **195,** 129 (2008).

[25] M. Espy *et al*., IEEE/CSC & ESAS European Superconductivity News Forum, No. 8 (2009).

[26] H.O. Meyer and P.T. Smith, Nucl. Instrum. Meth. **A647**, 117 (2011).

[27] J.M. Pendlebury, *et al*., Phys. Rev. **A70**, 032102 (2004);
A.L. Barabanov, R. Golub, and S.K. Lamoreaux, Phys. Rev. **A74**, 052115 (2006);
S.K. Lamoreaux and R. Golub, Phys. Rev. **A71**, 032104 (2005);
H. Yan and B. Plaster, Nucl. Instrum. Methods **A642**, 84 (2011).

[28] A. Esler *et al*., Phys. Rev. **C76**, 051302(R) (2007).

[29] P.H. Chu *et al*., Phys. Rev. **C84**, 022501(R) (2011).

[30] C.M. Swank, A. Petukhov, R. Golub, arXiv:1108.4701v1 [physics.data-an] (2011).